

Structural study of an amorphous NiZr₂ alloy by anomalous wide angle X-ray scattering and Reverse Monte Carlo simulations

J. C. de Lima,* D. Raoux, J. M. Tonnerre, and D. Udln
LURE Bât. 209D, Faculté des Sciences, Orsay 91405, France

K. D. Machado,† T. A. Grandi, and C. E. M. de Campos
Departamento de Física, Universidade Federal de Santa Catarina, 88040-900 Florianópolis, SC, Brazil

T. I. Morrison
CSRRI, 3101 South Dearborn Street Room 166 Life Sciences, Chicago, IL 60616
(Dated: November 6, 2018)

The local atomic structure of an amorphous NiZr₂ alloy was investigated using the anomalous wide-angle x-ray scattering (AWAXS), differential anomalous scattering (DAS) and reverse Monte Carlo (RMC) simulations techniques. The AWAXS measurements were performed at eight different incident photon energies, including some close to the Ni and Zr K edges. From the measurements eight total structure factor $\mathcal{S}(K, E)$ were derived. Using the AWAXS data four differential structure factors $DSF_i(K, E_m, E_n)$ were derived, two about the Ni and Zr edges. The partial structure factors $\mathcal{S}_{\text{Ni-Ni}}(K)$, $\mathcal{S}_{\text{Ni-Zr}}(K)$ and $\mathcal{S}_{\text{Zr-Zr}}(K)$ were estimated by using two different methods. First, the $\mathcal{S}(K, E)$ and $DSF_i(K, E_m, E_n)$ factors were combined and used in a matrix inversion process. Second, three $\mathcal{S}(K, E)$ factors were used as input data in the RMC technique. The coordination numbers and interatomic distances for the first neighbors extracted from the partial structure factors obtained by these two methods show a good agreement. By using the three-dimensional structure derived from the RMC simulations, the bond-angle distributions were calculated and they suggest the presence of distorted triangular-faced polyhedral units in the amorphous NiZr₂ structure. We have used the Warren chemical short-range order parameter to evaluate the chemical short-range order for the amorphous NiZr₂ alloy and for the NiZr₂ compound. The calculated values show that the chemical short-range order found in these two materials is similar to that found in a solid solution.

PACS numbers: 61.10.Eq, 61.43.Bn, 05.10.Ln, 81.15.Cd

I. INTRODUCTION

Amorphous materials have a great potential for application in technological devices, but their uses are limited due to several factors. One of them is the difficulty to obtain information about their atomic structures. Since most chemical and physical properties of these materials are defined by the first neighbors, knowledge of their structures becomes necessary. Due to the lack of translational symmetry, the determination of their atomic structures involves the combination of different diffraction and spectroscopic techniques as well as simulations and modeling.

The structure of an amorphous binary alloy is described by three pair correlation functions $G_{ij}(r)$, which are the Fourier transformation of the three partial structure factors $\mathcal{S}_{ij}(K)$. The total structure factor $\mathcal{S}(K, E)$, which can be derived from scattering measurements, is a weighted sum of these three $\mathcal{S}_{ij}(K)$ factors¹. Thus, to determine the three partial $\mathcal{S}_{ij}(K)$ at least three independent $\mathcal{S}(K, E)$ factors are needed. Usually, the following methods have been used to obtain these $\mathcal{S}(K, E)$ factors:

1. Isomorphous substitution: in this method one component of the amorphous alloy is substituted by a (expected) chemically similar one. For example, in amorphous Ni-Zr alloys the Zr atoms are replaced

by Hf atoms or the Ni atoms are partially substituted by Co or Fe atoms². This method is not very accurate since one cannot be sure of the chemical similarity of the two elements involved.

2. Isotope substitution: in this method one component of the amorphous alloy is substituted by an isotope or by an isotopic mixture and the scattering measurements are carried out using neutron sources. For example, in amorphous Ni-Zr alloys the Ni atoms are replaced by a Ni isotope³. The advantages of this method are limited by the availability of adequate isotopes.

With the development of the synchrotron radiation sources, anomalous wide angle x-ray scattering (AWAXS) and differential anomalous scattering (DAS) techniques became available for structural study of multicomponent disordered materials. AWAXS utilizes an incident radiation that is tuned close to an atomic absorption edge so that it interacts resonantly with the electrons of that particular atom. The atomic scattering factor of each chemical component can therefore be varied individually and the chemical environment about each component in the material can be investigated. Thus, in the case of an amorphous binary alloy, by using only one sample three independent $\mathcal{S}(K, E)$ factors can be obtained. However, the matrix formed by the weights of the three $\mathcal{S}(K, E)$

factors is ill-conditioned, becoming difficult the determination of the three $\mathcal{S}_{ij}(K)$ factors.

Fuoss^{4,5} tried to overcome this difficulty by implementing the DAS approach, which was proposed by Schevick^{6,7}. The DAS approach consists in taking the difference between the scattering patterns measured at two incident photon energies just below the edge of a particular atom, so that all correlation not involving this atom subtract out since only the atomic scattering factor of this atom changes appreciably. Later, De Lima *et al.*⁸, following a suggestion made by Munro⁹, combined the differential scattering factors $DSF_i(K, E_m, E_n)$ and the $\mathcal{S}(K, E)$ factors. They observed that this combination reduces the conditioning number of the matrix formed by the weights of these factors, allowing more stable values of $\mathcal{S}_{ij}(K)$ to be obtained.

The reverse Monte Carlo (RMC) simulation technique^{10,11,12,13} has been successfully used for structural modeling of amorphous structures. $\mathcal{S}(K, E)$ factors or their Fourier transformations, the total reduced radial distribution functions $G(r)$, can be used as input data. Applications of this technique to polymeric¹⁴, crystalline¹⁵ and amorphous^{16,17,18,19,20,21,22,23,24,25,26,27} materials are described in the literature.

In this paper, we report the determination of the three $\mathcal{S}_{ij}(K)$ factors obtained for amorphous NiZr₂ alloy by two independent ways: by making a combination of AWAXS and DAS techniques and also by combining AWAXS and RMC simulations techniques.

II. THEORETICAL BACKGROUND

A. Total and partial structure factors

According to Faber and Ziman¹, the $\mathcal{S}(K, E)$ factor is obtained from the scattered intensity per atom $I_a(K, E)$ as follows:

$$\begin{aligned} \mathcal{S}(K, E) &= \frac{I_a(K, E) - [\langle f^2(K, E) \rangle - \langle f(K, E) \rangle^2]}{\langle f(K, E) \rangle^2}, \\ &= \sum_{i=1}^n \sum_{j=1}^n W_{ij}(K, E) \mathcal{S}_{ij}(K), \end{aligned} \quad (1)$$

where K is the transferred momentum, E is the incident photon energy, $\mathcal{S}_{ij}(K)$ are the partial structure factors and $W_{ij}(K, E)$ are given by

$$W_{ij}(K, E) = \frac{c_i c_j f_i(K, E) f_j(K, E)}{\langle f(K, E) \rangle^2}, \quad (2)$$

and

$$\begin{aligned} \langle f^2(K, E) \rangle &= \sum_i c_i f_i^2(K, E), \\ \langle f(K, E) \rangle^2 &= \left[\sum_i c_i f_i(K, E) \right]^2. \end{aligned}$$

Here, c_i is the concentration and $f_i(K, E) = f_0(K) + f'(E) + i f''(E)$ is the atomic scattering factor of the component of type i and $f'(E)$ and $f''(E)$ are the anomalous dispersion terms. The total reduced distribution function $G(r)$ is related to the $\mathcal{S}(K, E)$ factor through the Fourier transformation

$$G(r) = \frac{2}{\pi} \int_0^\infty K [\mathcal{S}(K, E) - 1] \sin(Kr) dK,$$

while the partial reduced distribution functions $G_{ij}(r)$ are related to the $\mathcal{S}_{ij}(K)$ by means of the Fourier transformation

$$G_{ij}(r) = \frac{2}{\pi} \int_0^\infty K [\mathcal{S}_{ij}(K) - 1] \sin(Kr) dK.$$

From $G_{ij}(r)$ the partial radial distribution functions RDF_{ij}(r) can be calculated by

$$\text{RDF}_{ij}(r) = 4\pi\rho_0 c_j r^2 + r G_{ij}(r).$$

Interatomic distances are obtained from the maxima of the $G_{ij}(r)$ functions and coordination numbers are calculated by integrating the peaks of the RDF_{ij}(r) functions.

B. Differential structure factors and differential radial distribution functions

By using the Faber and Ziman formalism¹, the $DSF_i(K, E_m, E_n)$ factor around the component i is obtained as follows

$$\begin{aligned}
DSF_i(K, E_m, E_n) &= \frac{[I_a(K, E_m) - I_a(K, E_n)] - [LS(K, E_m) - LS(K, E_n)]}{\langle f(K, E_m) \rangle^2 - \langle f(K, E_n) \rangle^2}, \\
&= \sum_j U_{ij}(K, E_m, E_n) \mathcal{S}_{ij}(K),
\end{aligned} \tag{3}$$

where

$$LS(K, E) = \langle f^2(K, E) \rangle - \langle f(K, E) \rangle^2,$$

is the Laue scattering term and

$$U_{ij}(K, E_m, E_n) = \frac{c_i c_j [f_i(K, E_m) f_j(K, E_m) - f_i(K, E_n) f_j(K, E_n)]}{\langle f(K, E_m) \rangle^2 - \langle f(K, E_n) \rangle^2}. \tag{4}$$

For $i \neq j$ the weight $U_{ij}(K, E_m, E_n)$ must be multiplied by 2. The differential distribution function $DDF_i(r)$ can

be calculated by

$$DDF_i(r) = 4\pi\rho r^2 + \frac{2r}{\pi} \int_0^\infty K [DSF_i(K, E_m, E_n) - 1] \sin(Kr) dK.$$

For a binary amorphous alloy, as compared to the total radial distribution function $RDF(r)$, which is a sum of three $RDF_{ij}(r)$ functions, this function is the sum of only two $RDF_{ij}(r)$ functions and is sensitive only to the environment around the atoms of type i . In this way it is similar to EXAFS, though there are important differences due to the different sections of K -space measured²⁸.

as seen in Eqs. 2 and 4. P_ℓ is a weight which allows us to vary the contribution of any $\mathcal{SF}_\ell(K)$ factor. Here, $P_\ell = 1, \forall \ell$, and $M = 12$. By taking the derivatives of the $\mathcal{F}(K)$ function with respect to the $\mathcal{S}_{ij}(K)$ factors and putting them equal zero a linear system formed by three equations can be found. These three linear equations can be written as a matrix equation through

C. The matrix inversion method

In order to determine the three $\mathcal{S}_{ij}(K)$ factors using the eight $\mathcal{S}(K, E)$ and four $DSF_i(K, E_m, E_n)$ factors, a least-squares method was used. First of all, we define the function

$$\tilde{\mathcal{S}} = \tilde{W} \tilde{\mathcal{S}}_{ij},$$

and by inverting this matrix equation the $\mathcal{S}_{ij}(K)$ can be found. There are several methods to invert a matrix, and we have adopted the Singular Value Decomposition (SVD) method²⁹.

$$\mathcal{F}(K) = \sum_{\ell=1}^M P_\ell \left[\mathcal{SF}_\ell(K) - \sum_{i=1}^2 \sum_{j=1}^2 h_{ij}^\ell(K) \mathcal{S}_{ij}(K) \right]^2.$$

D. The RMC method

For $1 \leq \ell \leq 8$, $\mathcal{SF}_\ell(K)$ indicates the $\mathcal{S}(K, E_\ell)$ factors and for $9 \leq \ell \leq 12$ it stands for the $DSF_i^\ell(K, E_m, E_n)$ factors, as defined by Eqs. 1 and 3. In the same way, for $1 \leq \ell \leq 8$, $h_{ij}^\ell(K)$ indicates the $W_{ij}(K, E_\ell)$ weights and for $9 \leq \ell \leq 12$ it stands for the $U_{ij}^\ell(K, E_m, E_n)$ weights,

The basic idea and the algorithm of the standard RMC method are described elsewhere^{10,11,12,13} and its application to different materials is reported in the literature^{14,15,16,17,18,19,20,21,22,23,24,25,26,27}. In the RMC procedure, a three-dimensional arrangement of atoms with the same density and chemical composition of the alloy is placed into a cell (usually cubic) with periodic

boundary conditions and the $G_{ij}^{\text{RMC}}(r)$ functions corresponding to it are directly calculated through

$$G_{ij}^{\text{RMC}}(r) = \frac{n_{ij}^{\text{RMC}}(r)}{4\pi\rho_0 r^2 \Delta r},$$

where $n_{ij}^{\text{RMC}}(r)$ is the number of atoms at a distance between r and $r + \Delta r$ from the central atom, averaged over all atoms. By allowing the atoms to move (one at each time) inside the cell, the $G_{ij}^{\text{RMC}}(r)$ functions can be changed and, as a consequence, the $\mathcal{S}_{ij}(K)$ and $\mathcal{S}^{\text{RMC}}(K)$ factors are changed. Thus, the $\mathcal{S}^{\text{RMC}}(K, E)$ factor is compared to the $\mathcal{S}(K, E)$ factor in order to minimize the differences between them. The function to be minimized is

$$\psi^2(E) = \frac{1}{\delta} \sum_{i=1}^m [\mathcal{S}(K_i, E) - \mathcal{S}^{\text{RMC}}(K_i, E)]^2,$$

where the sum is over m experimental points and δ is related to the experimental error in $\mathcal{S}(K, E)$. If the movement decreases ψ^2 , it is always accepted. If it increases ψ^2 , it is accepted with a probability given by $\exp(-\Delta\psi^2/2)$; otherwise it is rejected. As this process is iterated ψ^2 decreases until it reaches an equilibrium value. Thus, the atomic configuration corresponding to equilibrium should be consistent with the experimental total structure factor within the experimental error. By using the $G_{ij}^{\text{RMC}}(r)$ functions and the $\mathcal{S}_{ij}^{\text{RMC}}(K)$ factors the coordination numbers and interatomic distances can be calculated. In addition, the bond-angle distributions can also be determined.

III. EXPERIMENTAL PROCEDURE

A. Sample and holder

Amorphous NiZr₂ thin films were prepared on a NaCl cooled substrate by the sputtering triode technique at the Argonne National Laboratory. In order to eliminate the substrate a metallic holder with a central rectangular hole was glued on the thin film, and the set was immersed in water to dissolve the NaCl substrate. The thickness and density of the thin films were 2 μm and 7.32 g/cm³, respectively.

B. Apparatus and data collection

The AWAXS scattering experiments were performed some years ago on the D4 beamline at LURE (Orsay - France) using the DCI synchrotron radiation source. All measurements were performed using a two-circles diffractometer in the vertical plane described elsewhere^{30,31} equipped with a two crystal Si (220) or Ge (400)

monochromator and a Si:Li energy sensitive detector which is sufficient to discriminate the large K_α resonant Raman/fluorescence signal when incident photon energy is tuned close to the Ni and Zr K edges but insufficient to distinguish the small elastic, K_β and Compton signals. The Si (220) and Ge (400) crystal monochromators were used to collect data around the Ni and Zr edges, respectively. The sample was sealed, under vacuum, into a cell containing a large kapton window fixed around the diffractometer horizontal rotation axis to reduce the air scattering. In order to take into account the time-decrease of the beam, the incident intensity I_0 was measured by placing a NaI photomultiplier tube between the monochromator and the diffractometer. Absorption measurements were performed on the Ni and Zr K edges for energy calibration. For each incident photon energy listed in Table I, the energy windows for K_α , resonant Raman/fluorescence, K_β , Compton, and elastic signals were defined by measuring the scattered intensities at two different angular positions: the beginning of the windows was defined at the lowest scattering angle and their ends at the highest one. Scattering patterns were collected using the symmetrical reflection geometry. To improve the quality of the data, at least four scattering measurements were performed at the incident photon energies shown in Table I.

TABLE I: f'_i and f''_i values used here.

Energy (eV)	f'_{Ni}	f''_{Ni}	f'_{Zr}	f''_{Zr}
8210	-3.895	0.491	-0.347	2.167
8330	-7.333	0.658	-0.367	2.167
9659	-0.964	3.051	-0.586	1.629
11867	-0.063	2.158	-0.950	1.126
16101	0.254	1.287	-1.985	0.648
17398	0.269	1.121	-2.999	0.563
17987	0.269	1.057	-7.371	0.734
19200	0.264	0.940	-1.953	3.315

C. Determination of the anomalous scattering factors

In order to interpret the scattering data correctly, the real and the imaginary parts f' and f'' of the atomic scattering factor were determined accurately following a procedure described by Dreier *et al.*³² X-ray absorption coefficients were measured over a broad energy range near the Ni and Zr K edges on the sample and f'' was calculated using the optical theorem. The absorption measurements were performed on the XAS beamline at LURE, in transmission mode, and two standard ionization chambers were used as the detecting system. Outside the region of measurement, theoretical values³³ of f'' were used to extend the experimental data set over a larger energy

range and f' was calculated using the Kramers-Kronig relation. For the measurements away from the K edges, the f' and f'' values were taken from a table compiled by Sasaki³⁴. The obtained values for the incident photon energies 8330 eV and 17987 eV are listed in Table I together with Sasaki values. The atomic scattering factor away from the K edge, $f_0(K)$, of neutral Ni and Zr atoms were calculating according to the analytic function given by Cromer and Mann³⁵.

D. Data analysis

Each scattering pattern was treated separately. Due to the diffractometer characteristics, the polarization correction was disregarded. The measured scattered intensities away from the Ni and Zr K edges were corrected for detector non-linearities and reabsorption effects being then put on a per atom scale and the Compton scattering eliminated. For those measured close to the Ni and Zr edges, besides the corrections above, the contribution of the K_β fluorescence to the elastic scattering was eliminated. This contribution was evaluated, after corrections for reabsorption effects, by using the K_β/K_α ratio, which was measured at an incident photon energy above the edge, because they were completely separated. Two method were tested to put the scattered intensities on a per atom scale: that described by Krogh-Moe-Norman^{36,37,38} and the one based on the high-angle procedure^{36,39}. For the elastic scattered intensity around the Zr edge, for which the K data range is larger ($K_{\max} \approx 13 \text{ \AA}^{-1}$), both method gave the same result. The K data range was reduced and the Krogh-Moe-Norman method was then applied. The normalized signal was identical to the one obtained previously. So, we have kept the Krogh-Moe-Norman method to put the scattered intensities on a per atom scale including those around the Ni edge, for which the K data range is smaller ($K_{\max} \approx 8 \text{ \AA}^{-1}$). The good quality of the total structure factors shown in Fig. 1 and 2 corroborates the accuracy of the procedure used. The Compton scattering contribution was calculated according to the analytic approximation given by Pálinkas⁴⁰.

IV. RESULTS AND DISCUSSION

A. Total structure factors, differential structure factors and differential distribution functions

Figures 1 and 2 show the $\mathcal{S}(K, E)$ factors for the incident photon energies described in Table I. The $\mathcal{S}(K, E)$ factors for the energies greater than 16101 eV (see Fig. 2) show a pre-peak located at about $K = 1.65 \text{ \AA}^{-1}$, which reaches the maximum intensity close to the Zr edge. It is absent in the $\mathcal{S}(K, E)$ factors for the smallest energies (see Fig. 1). Since $\mathcal{S}(K, E)$ is a weighted sum of $\mathcal{S}_{ij}(K)$, we calculated the weights $W_{ij}(K, E)$ for the $\mathcal{S}_{\text{Ni-Ni}}(K)$,

$\mathcal{S}_{\text{Ni-Zr}}(K)$ and $\mathcal{S}_{\text{Zr-Zr}}(K)$ factors. Their contributions for the $\mathcal{S}(K, E)$ factor at 8330 eV are about 4%, 32% and 64% while for the $\mathcal{S}(K, E)$ factor at 17987 eV they are about 10%, 43% and 47%, respectively. Thus, the determination of Ni-Ni first neighbors is more difficult than for the Ni-Zr and Zr-Zr first neighbors.

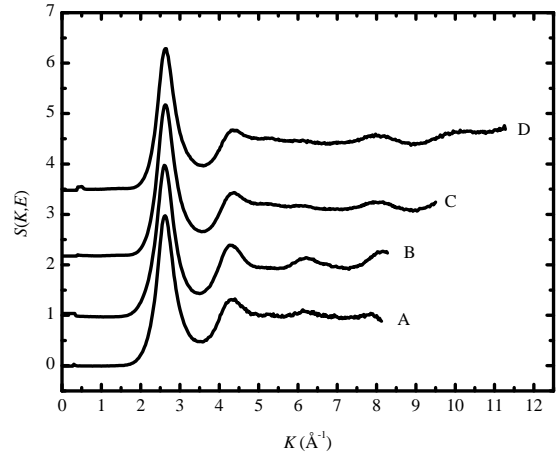


FIG. 1: $\mathcal{S}(K, E)$ factors for energies $E_1 = 8210 \text{ eV}$ (A), $E_2 = 8330 \text{ eV}$ (B), $E_3 = 9659 \text{ eV}$ (C) and $E_4 = 11867 \text{ eV}$ (D).

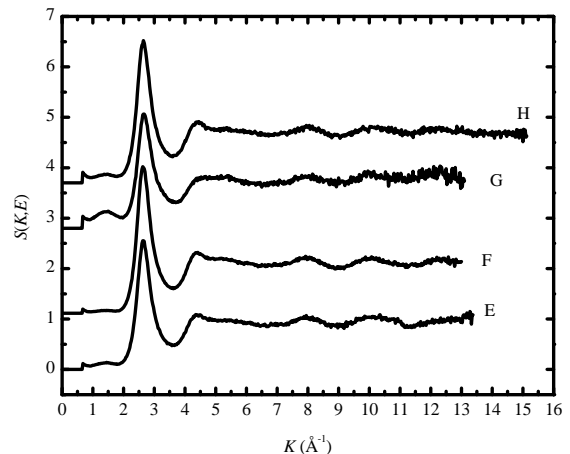


FIG. 2: $\mathcal{S}(K, E)$ factors for energies $E_5 = 16101 \text{ eV}$ (E), $E_6 = 17398 \text{ eV}$ (F), $E_7 = 17987 \text{ eV}$ (G) and $E_8 = 19200 \text{ eV}$ (H).

We have used the scattered intensities on a per atom scale obtained at the incident photon energy pairs (8210, 8330 eV), (8330, 9659 eV), (16101, 17987 eV) and (17987, 19200 eV) to calculate four $DSF_i(K, E_m, E_n)$ factors around the Ni and Zr atoms. Figures 3 and 4 show them and their $DDF_i(r)$ functions. Figure 3 shows that the chemical environment around Ni and Zr atoms is very different. For instance, it is seen a broad shoulder on the right side of the first peak in the $DSF_{\text{Ni}}(K, E_m, E_n)$ factors which is absent in the $DSF_{\text{Zr}}(K, E_m, E_n)$ factors. The $DDF_{\text{Zr}}(r)$ functions show the first coordination shell split into two subshells, located at about

$r = 2.64 \text{ \AA}$ and 3.23 \AA , while the $DDF_{\text{Ni}}(r)$ functions display the first coordination shell located at a mean distance $r = 2.77 \text{ \AA}$. The contribution of the Ni-Ni and Ni-Zr pairs to them is not resolved. This can be related to the small K data range of the measured scattered intensities. The weight $U_{\text{Ni-Ni}}(K)$ to the $DSF_{\text{Ni}}(K, E_m, E_n)$ factor is about 25%, and it is almost four times larger than the weight $W_{\text{Ni-Ni}}(K)$ for the $\mathcal{S}(K, E)$ factors, allowing a more realistic determination of the number of Ni-Ni first neighbors.

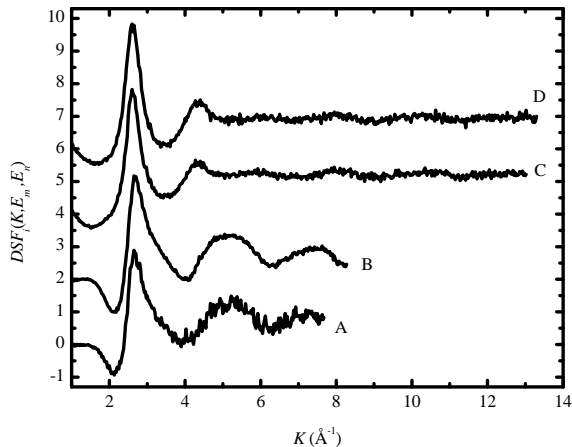


FIG. 3: $DSF_i(K, E_m, E_n)$ factors. $DSF_{\text{Ni}}(K, E_m, E_n)$ for energies (E_1, E_2) (A) and (E_2, E_3) (B). $DSF_{\text{Zr}}(K, E_m, E_n)$ for energies (E_5, E_7) (C) and (E_7, E_8) (D).

By considering the atomic radius of Ni and Zr atoms, the subshells located at the distances $r = 2.64 \text{ \AA}$ and 3.23 \AA in the $DDF_{\text{Zr}}(r)$ functions were directly attributed to Zr-Ni and Zr-Zr correlations. This fact allowed us to deconvolute their first shells and, consequently, also the first shells of the $DDF_{\text{Ni}}(r)$ functions, by assuming a Gaussian shape for them. To do this, we explicitly took into

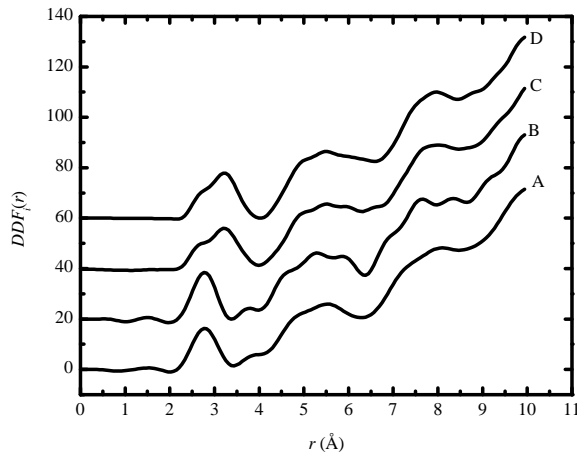


FIG. 4: $DDF_i(r)$ functions. $DDF_{\text{Ni}}(r)$ for energies (E_1, E_2) (A) and (E_2, E_3) (B). $DDF_{\text{Zr}}(r)$ for energies (E_5, E_7) (C) and (E_7, E_8) (D).

TABLE II: Structural parameters determined for the a -NiZr₂ alloy.

Deconvolution of $DDF_i(r)$ functions							
Bond Type	Ni-Ni	Ni-Zr	Zr-Ni	Zr-Zr			
N	1.3	8.4	4.2	11.6			
r (Å)	2.67	2.67	2.76	3.21			
Matrix inversion							
Bond Type	Ni-Ni	Ni-Zr	Zr-Ni	Zr-Zr			
N	2.3	7.5	3.8	10.8			
r (Å)	2.64	2.77	2.77	3.24			
RMC							
Bond Type	Ni-Ni	Ni-Zr ^a	Zr-Ni ^b	Zr-Zr			
N	3.2	6.9	2.3	3.5	1.1	10.1	
r (Å)	2.68	2.73	3.62	2.73	3.62	3.25	
Crystalline NiZr ₂ compound							
Bond Type	Ni-Ni	Ni-Zr	Zr-Ni	Zr-Zr ^c			
N	2.0	8.0	4.0	1.0	2.0	4.0	4.0
r (Å)	2.63	2.79	2.79	2.82	3.17	3.30	3.47
Amorphous Ni ₃₅ Zr ₆₅ alloy ²							
Bond Type	Ni-Ni	Ni-Zr	Zr-Ni	Zr-Zr			
N	3.3	8.6	4.8	11.0			
r (Å)	2.45	2.85	2.85	3.30			
Amorphous Ni ₃₆ Zr ₆₄ alloy ³							
Bond Type	Ni-Ni	Ni-Zr	Zr-Ni	Zr-Zr			
N	2.3	7.9	3.9	9.1			
r (Å)	2.66	2.69	2.69	3.15			

^aThere are 9.2 Ni-Zr pairs at $\langle r \rangle = 2.95 \text{ \AA}$.

^bThere are 4.6 Zr-Ni pairs at $\langle r \rangle = 2.95 \text{ \AA}$.

^cThere are 11 Zr-Zr pairs at $\langle r \rangle = 3.29 \text{ \AA}$.

account the K dependence by Fourier transforming into the K space the Gaussian distributions multiplied by the weights $U_{ij}(K, E_m, E_n)$ and back Fourier transforming over the same K range used to calculate the $DDF_i(r)$. The structural parameters extracted from the deconvolution are listed in Table II.

B. Partial structure factors obtained from the matrix inversion and RMC methods

1. Partial $\mathcal{S}_{ij}(K)$ factors obtained from the matrix inversion method

By considering the eight $\mathcal{S}(K, E)$ and the four $DSF_i(K, E_m, E_n)$ factors, a reduction of a factor of 15 (at $K = 1.65 \text{ \AA}^{-1}$) and 7 (at $K = 7.65 \text{ \AA}^{-1}$) in the conditioning number of the matrix \tilde{W} was reached when compared to the use of the eight $\mathcal{S}(K, E)$ factors only. To obtain the three $\mathcal{S}_{ij}(K)$ factors, the $\mathcal{S}(K, E)$ and $DSF_i(K, E_m, E_n)$ factors were restricted to $K_{\text{max}} = 7.65$

\AA^{-1} . The $\mathcal{S}_{\text{Ni-Ni}}(K)$, $\mathcal{S}_{\text{Ni-Zr}}(K)$ and $\mathcal{S}_{\text{Zr-Zr}}(K)$ factors (thin lines) obtained are shown in Fig. 5. From this figure, the $\mathcal{S}_{\text{Ni-Zr}}(K)$ and $\mathcal{S}_{\text{Zr-Zr}}(K)$ factors seem to be of good quality, specially between $K = 1.5 \text{ \AA}^{-1}$ and $K = 3.5 \text{ \AA}^{-1}$, where the conditioning number presents the largest changes. On the other hand, the $\mathcal{S}_{\text{Ni-Ni}}(K)$ factor displays a minimum apparently without physical meaning in this region. The $\mathcal{S}_{\text{Ni-Zr}}(K)$ factor shows a minimum at $K = 2.2 \text{ \AA}^{-1}$, which was already observed in the $DSF_{\text{Ni}}(K, E_m, E_n)$ factors, while the $\mathcal{S}_{\text{Zr-Zr}}(K)$ factor displays a shoulder at this K value. Although the $\mathcal{S}_{\text{Ni-Ni}}(K)$ factor is very noisy, it is possible to see a weak pre-peak at about $K = 1.5 \text{ \AA}^{-1}$ which was already observed in the $\mathcal{S}(K, E)$ factors around the Zr edge and also some weak halos beyond $K = 3.5 \text{ \AA}^{-1}$.

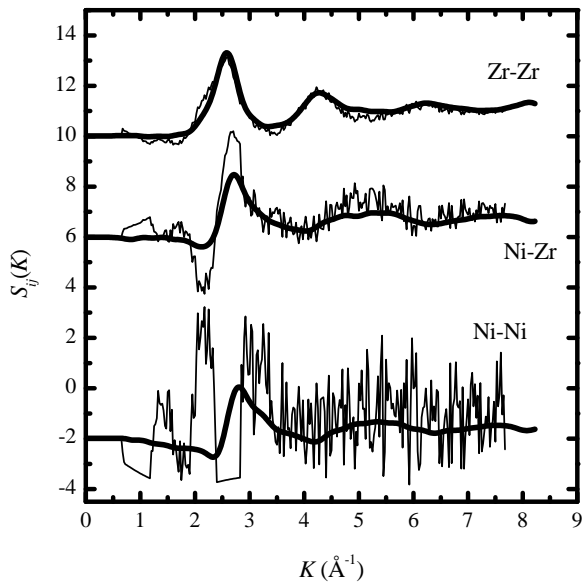


FIG. 5: $\mathcal{S}_{\text{Ni-Ni}}(K)$, $\mathcal{S}_{\text{Ni-Zr}}(K)$ and $\mathcal{S}_{\text{Zr-Zr}}(K)$ factors obtained from the matrix inversion (thin lines) and RMC simulations (thick lines) techniques.

Figure 6 shows the $\text{RDF}_{ij}(r)$ functions (thin lines) obtained by Fourier transformation of the $\mathcal{S}_{ij}(K)$ factors. From this picture one can see that the $\text{RDF}_{\text{Ni-Ni}}(r)$ function shows a very weak first coordination shell, located at about $r = 2.64 \text{ \AA}$, while the second and third ones, located at about $r = 4.5 \text{ \AA}$ and 6.7 \AA , respectively, are very intense. The $\text{RDF}_{\text{Ni-Zr}}(r)$ function displays a well isolated first coordination shell, located at about $r = 2.77 \text{ \AA}$; a small shoulder at about $r = 3.83 \text{ \AA}$, and well defined and intense second and third coordination shells, located at about $r = 5.4 \text{ \AA}$ and 7.9 \AA . The $\text{RDF}_{\text{Zr-Zr}}(r)$ function shows the first coordination shell well isolated, located at about $r = 3.3 \text{ \AA}$; the second one splits into two subshells, located at about $r = 5.18 \text{ \AA}$ and 6.35 \AA , which are very weak. The interatomic distances and coordination numbers for the first neighbors obtained from these functions are listed in Table II.

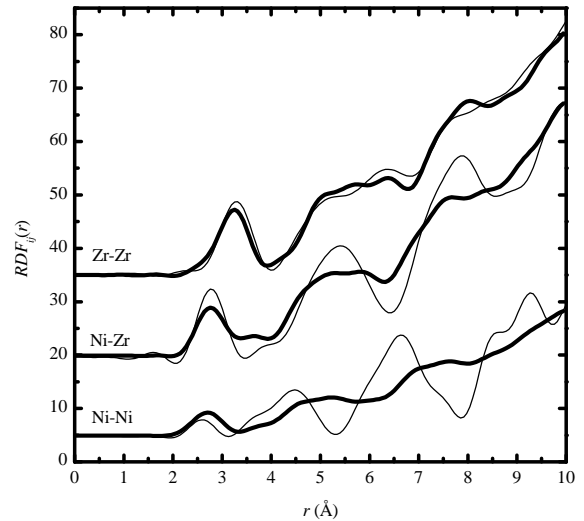


FIG. 6: $\text{RDF}_{\text{Ni-Ni}}(r)$, $\text{RDF}_{\text{Ni-Zr}}(r)$ and $\text{RDF}_{\text{Zr-Zr}}(r)$ functions obtained from the matrix inversion (thin lines) and RMC simulations (thick lines) techniques.

2. Partial $\mathcal{S}_{ij}(K)$ obtained from the RMC simulations

In order to perform the simulations we have considered a cubic cell with 1800 atoms (600 Ni and 1200 Zr), $\delta = 0.01$, and a mean atomic number density $\rho_0 = 0.054719 \text{ atoms/\AA}^3$. The minimum distances between atoms were fixed at the beginning of the simulations at $r_{\text{Ni-Ni}} = 2.2 \text{ \AA}$, $r_{\text{Ni-Zr}} = 2.4 \text{ \AA}$ and $r_{\text{Zr-Zr}} = 2.6 \text{ \AA}$. To make the simulations we used the RMC programs available at the Internet¹². The $\mathcal{S}(K, E)$ factors obtained at the photon energies 8330 eV, 17398 eV and 19200 eV were used as input data. These $\mathcal{S}(K, E)$ factors were cut at the same K value. The $\mathcal{S}(K, E)$ (solid lines) and $\mathcal{S}^{\text{RMC}}(K, E)$ factors (square lines) are shown in Fig. 7 and they show a good agreement.

The $\mathcal{S}_{ij}^{\text{RMC}}(K)$ factors (thick lines) are also shown in Fig. 5, together with those obtained from the matrix inversion method. The agreement among them is very good, mainly for the $\mathcal{S}_{\text{Zr-Zr}}(K)$ factor. For instance, the shoulder previously observed in $\mathcal{S}_{\text{Zr-Zr}}(K)$ factor and the peaks located around $K = 2.58 \text{ \AA}^{-1}$, 4.3 \AA^{-1} and 6.2 \AA^{-1} are also seen in the $\mathcal{S}_{\text{Zr-Zr}}^{\text{RMC}}(K)$ factor; the minimum at $K = 2.1 \text{ \AA}^{-1}$ and peaks around $K = 2.7 \text{ \AA}^{-1}$, 5.2 \AA^{-1} and 7.6 \AA^{-1} observed in the $\mathcal{S}_{\text{Ni-Zr}}(K)$ are also seen in the $\mathcal{S}_{\text{Ni-Zr}}^{\text{RMC}}(K)$ factor; and it is interesting to note that the minimum previously observed in the $\mathcal{S}_{\text{Ni-Ni}}(K)$ factor is now replaced by a well defined maximum in the $\mathcal{S}_{\text{Ni-Zr}}^{\text{RMC}}(K)$ factor. Other peaks observed before in the $\mathcal{S}_{\text{Ni-Ni}}(K)$ factor are also seen in the $\mathcal{S}_{\text{Ni-Ni}}^{\text{RMC}}(K)$ factor. The $\text{RDF}_{ij}^{\text{RMC}}(r)$ functions (thick lines) are also shown in Fig. 6. The interatomic distances and coordination numbers for the first neighbors extracted from the $G_{ij}^{\text{RMC}}(r)$ and $\text{RDF}_{ij}^{\text{RMC}}(r)$ functions are also listed in Table II.

It is interesting to note that although we have used eight independent $\mathcal{S}(K, E)$ and four $DSF_i(K, E_m, E_n)$

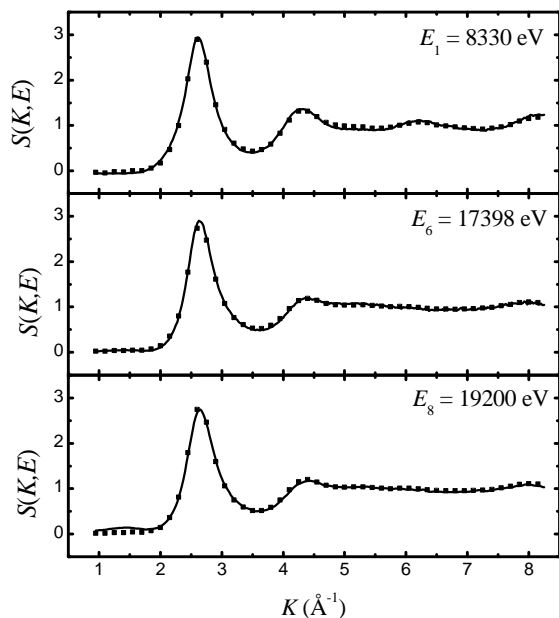


FIG. 7: $S(K, E)$ (full lines) and $S^{\text{RMC}}(K, E)$ (squares) factors for the amorphous NiZr_2 alloy.

factors to obtain the three $\mathcal{S}_{ij}(K)$ factors by the matrix inversion method, the $\mathcal{S}_{\text{Ni-Ni}}(K)$ factor shows a minimum between $K = 1.5 \text{ \AA}^{-1}$ and 3.5 \AA^{-1} which have no physical meaning. On the other hand, using only three $S(K, E)$ factors as input data in the RMC method we have obtained excellent results, even for the $\mathcal{S}_{\text{Ni-Ni}}(K)$ factor.

In a previous study, Lee *et al.*² and Mizoguchi *et al.*³ reported the $\mathcal{S}_{ij}(K)$ factors obtained for the amorphous $\text{Ni}_{35}\text{Zr}_{65}$ and $\text{Ni}_{36}\text{Zr}_{64}$ alloys, respectively. Lee *et al.* used alloys containing mixtures of Co and Fe in small quantities while Mizoguchi *et al.* used the isotopic substitution method. A comparison among the $\mathcal{S}_{ij}^{\text{RMC}}(K)$, $G_{ij}^{\text{RMC}}(r)$ and $\text{RDF}_{ij}^{\text{RMC}}(r)$ functions obtained in this work, by using only one sample, with those reported by them shows that they are in a good agreement.

By defining the partial bond-angle distribution functions $\Theta_{i-j-l}(\cos\theta)$ where j is the atom in the corner, we calculated the angular distribution of the bonds between first neighbor atoms. The six $\Theta_{i-j-l}(\cos\theta)$ functions found are shown in Fig. 8. This kind of information cannot be obtained by the matrix inversion method because the partial distribution functions give only a one-dimensional description of the atomic arrangement.

Hausleitner and Hafner⁴¹ investigated several amorphous alloys formed by transition metals using molecular dynamics simulations. They obtained the structure factors, coordination numbers, interatomic distances and also the bond-angle distribution functions. According to them, if the components of an alloy have a large difference in the number of d electrons there is a pronounced non-additivity of the pair interactions and a strong interaction between unlike atoms. Therefore, in certain amorphous

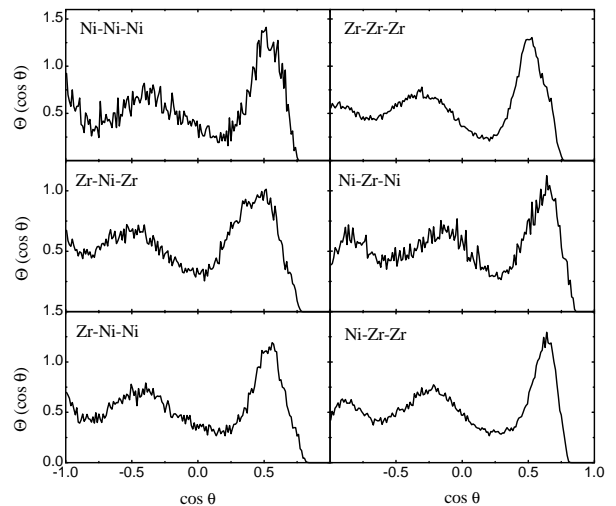


FIG. 8: $\Theta_{i-j-l}(\cos\theta)$ functions obtained by the RMC simulations.

alloys the interatomic distance of heteropolar bonds can be shorter than the distance of homopolar ones^{23,42}. This also favors the formation of trigonal-prismatic units. The shortening effect was not observed in this study. The bond angle values of triangular and square faces of a distorted prism are found around $\theta = 60^\circ$, 90° – 100° , 109° and 147° . Thus, the bond angle values shown in Fig. 8 suggest that distorted polyhedral units with triangular faces are present in the atomic structure of the amorphous NiZr_2 alloy and if there are square-faced polyhedral units, they are found in a very small quantity. The presence of this kind of units was already reported in amorphous $\text{Ni}_{60}\text{Ti}_{40}$ ²³, $\text{Ni}_{33}\text{Ti}_{67}$ ²⁵, $\text{Pd}_{82}\text{Si}_{18}$ ²⁶ and $\text{Ni}_{65}\text{B}_{35}$ ²⁷ alloys.

Havinga *et al.*⁴³ reported crystallographic data for several compounds with CuAl_2 (C16)-type structure. We have used their data for the NiZr_2 compound in the CRYSTAL OFFICE98 software⁴⁴ to obtain the interatomic distances and coordination numbers for the first neighbors listed in Table II. Its structure has angles around $\theta = 53$ – 56° , 64° , 96 – 112° and 143 – 154° . For the amorphous NiZr_2 alloy the $\Theta_{i-\text{Zr}-l}(\cos\theta)$ functions (i and l can be Ni or Zr atoms) found are very similar to those present in the NiZr_2 compound. On the other hand, the $\Theta_{i-\text{Ni}-l}(\cos\theta)$ functions show some important differences. The Ni–Ni–Ni sequence in the compound is linear ($\theta = 180^\circ$) while in amorphous NiZr_2 alloy it can also be found at triangular angles ($\theta = 60^\circ$ and 112°); the Zr–Ni–Ni and Zr–Ni–Zr sequences found in the amorphous NiZr_2 alloy show bond angles around $\theta = 180^\circ$ that are not found in the compound. These data suggest that in the amorphous alloy the local structure around a Ni atom can be more distorted than around a Zr atom.

The chemical short-range order parameter is a quantitative measurement of the degree of chemical short-range order. There are several definitions of chemical short-range order parameters⁴⁵. We have adopted the War-

ren chemical short-range order (CSRO) parameter α_1 ⁴⁶ given below to compare the amorphous NiZr₂ alloy and the NiZr₂ compound.

$$\alpha_1 = 1 - \frac{N_{12}^1}{c_2(c_1 N_2^1 + c_2 N_1^1)}, \quad (5)$$

Here, $N_{12}^1 = N_{\text{Ni-Zr}}$ and $N_1^1 = N_{\text{Ni-Ni}} + N_{\text{Ni-Zr}}$ and $N_2^1 = N_{\text{Zr-Zr}} + N_{\text{Zr-Ni}}$ are the total coordination numbers in the first shell. By using the coordination numbers given in Table II, we found $\alpha_1^{\text{RMC}} = -0.029$ and for the compound $\alpha_1^{\text{NiZr}_2} = -0.024$. The chemical short-range order in the amorphous NiZr₂ alloy is similar to that found in a solid solution, for which $\alpha_1 = 0$. The same behavior is observed in the NiZr₂ compound.

V. CONCLUSION

The amorphous NiZr₂ alloy was investigated by using AWAXS, DAS and RMC simulations techniques. The three $\mathcal{S}_{ij}(K)$ factors were determined by using two independent ways: a combination of AWAXS and DAS techniques and by combining AWAXS and RMC simulations techniques. The $\mathcal{S}_{\text{Ni-Zr}}(K)$ and $\mathcal{S}_{\text{Zr-Zr}}(K)$ factors obtained by both combinations showed an excellent agreement, but the simulations gave the best result for the $\mathcal{S}_{\text{Ni-Ni}}(K)$ factor. The coordination numbers and interatomic distances calculated from the RDF_{*ij*}(*r*) func-

tions obtained by these two combinations show a good agreement among themselves and with those extracted from the deconvolution of the $DDF_{\text{Ni}}(r)$ and $DDF_{\text{Zr}}(r)$ functions.

The results achieved in this study suggest that the combination of the RMC simulations method and AWAXS can be used to obtain more reliable $\mathcal{S}_{ij}(K)$ factors than those obtained by the matrix inversion method, in particular for the Ni-Ni pairs, which have the smallest weighting factor. This was already observed in a neutron diffraction study performed in a CuBr alloy⁴⁷, which is also an ill-conditioned problem similar to ours. In addition, this combination gives us some evidence of the presence of distorted polyhedral units with triangular faces in the atomic structure of the amorphous NiZr₂ alloy.

The calculated Warren CSRO parameter indicated that the chemical short-range order found in the amorphous NiZr₂ alloy is similar to that found in a solid solution, and there is some resemblance with that found in the NiZr₂ compound.

Acknowledgments

Two of the authors, J. C. De Lima and K. D. Machado, would like to thank the Conselho Nacional de Desenvolvimento Científico e Tecnológico (CNPq), Brazil, for financial support.

-
- * Electronic address: fsc1jcd@fisica.ufsc.br; Permanent address: Departamento de Física, Universidade Federal de Santa Catarina, 88040-900 Florianópolis, SC, Brazil
- † Electronic address: kleber@fisica.ufsc.br
- ¹ T. E. Faber and J. M. Ziman, *Philos. Mag.* **11** (1965).
 - ² A. E. Lee, S. Jost, C. N. J. Wagner, and L. E. Tanner, *J. Physique* **46**, C8 (1985).
 - ³ T. Mizoguchi, S. Yoda, N. Akutsu, S. Yamada, S. Nishioka, T. Suenara, and N. Watanabe, *Rapid Quenched Materials* **51**, 483 (1985).
 - ⁴ P. Fuoss, SSRL Report **80/06** (1980).
 - ⁵ P. H. Fuoss, P. Eisenberger, W. Warburton, and A. Bienenstock, *Phys. Rev. Lett.* **46**, 1537 (1981).
 - ⁶ N. J. Shevchik, *Philos. Mag.* **35**, 805 (1977).
 - ⁷ N. J. Shevchik, *Philos. Mag.* **35**, 1289 (1977).
 - ⁸ J. C. de Lima, J. M. Tonnerre, and D. Raoux, *J. Non-Cryst. Solids* **106**, 38 (1988).
 - ⁹ R. Munro, *Phys. Rev. B* **25**, 5037 (1982).
 - ¹⁰ R. L. McGreevy and L. Pusztai, *Mol. Simulations* **1**, 359 (1988).
 - ¹¹ R. L. McGreevy, *Nuc. Inst. & Met. in Phys. Res. A* **354**, 1 (1995).
 - ¹² RMCA version 3, R. L. McGreevy, M. A. Howe and J. D. Wicks, 1993. available at <http://www.studsvik.uu.se>.
 - ¹³ R. L. McGreevy, *J. Phys.: Condens. Matter* **13**, 877 (2001).
 - ¹⁴ B. Rosi-Schwartz and G. R. Mitchell, *Polymer* **35**, 5398 (1994).
 - ¹⁵ A. Mellergard and R. L. McGreevy, *Acta Cryst. A* **55**, 783 (1999).
 - ¹⁶ L. Karlsson, A. Wannberg, and R. L. McGreevy, *Phys. Rev. B* **61**, 487 (2000).
 - ¹⁷ P. Jónvári and L. Pusztai, *Phys. Rev. B* **64** (2001).
 - ¹⁸ D. A. Keen and R. L. McGreevy, *Nature* **344**, 423 (1990).
 - ¹⁹ Y. Wang, K. Lu, and C. Li, *Phys. Rev. Lett.* **79** (1997).
 - ²⁰ M. Bionducci, G. Navarra, R. Bellisent, G. Concas, and F. Congiu, *J. Non-Cryst. Solids* **250**, 605 (1999).
 - ²¹ J. D. Wicks and R. L. McGreevy, *J. Non-Cryst. Solids* **192**, 23 (1995).
 - ²² A. D. Cicco, M. Taglienti, M. Minicucci, and A. Filipponi, *Phys. Rev. B* **62**, 12001 (2000).
 - ²³ K. D. Machado, J. C. de Lima, C. E. M. de Campos, T. A. Grandi, and D. M. Trichês, *Phys. Rev. B* **66** (2002).
 - ²⁴ C. Tengroth, J. Swenson, A. Isopo, and L. Borjesson, *Phys. Rev. B* **64**, 4207 (2001).
 - ²⁵ E. W. Iparraguirre, J. Sietsma, and B. J. Thijsse, *J. Non-Cryst. Solids* **156–158**, 969 (1993).
 - ²⁶ T. Ohkubo, H. Kai, and Y. Hirotsu, *Mat. Sci. Eng. A* **304–306**, 300 (2001).
 - ²⁷ L. Pusztai and E. Sváb, *J. Phys.: Condens. Matter* **5**, 8815 (1993).
 - ²⁸ J. Kortwright, W. K. Warburton, and A. Bienenstock, *EXAFS and Near Edge Structure, Proceedings of the Int. Conf. Frascati, Italy* (Springer, Berlin, 1982).
 - ²⁹ W. H. Press, S. A. Teukolsky, B. P. Flannery, and W. T.

- Vetterling, *Numerical Recipes - The Art of Scientific Computing* (Cambridge University Press, New York, 1986).
- ³⁰ M. Laridjani, D. Raoux, P. Leboucher, and J. Sadoc, *J. Physique* **C8**, 157 (1985).
- ³¹ M. Laridjani, J. F. Sadoc, and D. Raoux, *J. Non-Cryst. Solids* **91**, 217 (1987).
- ³² P. Dreier, P. Rabe, W. Malzfeldt, and W. Niemann, *J. Phys. C: Solid State Phys.* **17**, 3123 (1984).
- ³³ W.H. McMaster, N. Kerr Del Grande, J.H. Mallett and J.H. Hubbell, UCRL-50174 Sec. II Rev. 1, National Bureau of Standards, distributed by Nat. Tech. Information Service, U.S. Department of Commerce.
- ³⁴ S. Sasaki, *Anomalous Scattering Factors for Synchrotron Radiation Users, Calculated using Cromer and Liberman's Method* (National Laboratory for High Energy Physics, Japan, 1984).
- ³⁵ D. T. Cromer and J. B. Mann, *Acta Cryst. A* **24**, 321 (1968).
- ³⁶ C. N. J. Wagner, *Liquid Metals* (S. Z. Beer, Marcel Dekker, New York, 1972).
- ³⁷ J. Krogh-Moe, *Acta Cryst.* **9**, 951 (1956).
- ³⁸ N. Norman, *Acta Cryst.* **10**, 370 (1957).
- ³⁹ N. S. Gingrich, *Rev. Mod. Phys.* **15**, 90 (1943).
- ⁴⁰ G. Pálinkas, *Acta Cryst. A* **29**, 10 (1973).
- ⁴¹ C. Hausleitner and J. Hafner, *Phys. Rev. B* **45**, 128 (1992).
- ⁴² T. Fukunaga, N. Watanabe, and K. Suzuki, *J. Non-Cryst. Solids* **61 & 62**, 343 (1984).
- ⁴³ E. E. Havinga, H. Damsma, and P. Hokkeling, *J. Less-Common Metals* **27**, 169 (1972).
- ⁴⁴ Atomic Softtek, 70 Longwood Road North, Hamilton, Ontario, Canada L8S 3V4.
- ⁴⁵ S. Steeb and P. Lamparter, *Ordering and Desordering in Alloys* (Elsevier, London, 1992).
- ⁴⁶ M. Maret, P. Chieux, P. Hicter, M. Atzmon, and W. L. Jonhson, *J. Phys. F: Met. Phys.* **17**, 315 (1987).
- ⁴⁷ L. Pusztai and R. McGreevy, *J. Phys.: Condens. Matter.* **10**, 525 (1998).